Atmos. Chem. Phys., 14, 5599–5615, 2014
www.atmos-chem-phys.net/14/5599/2014/
doi:10.5194/acp-14-5599-2014

Atmospheric Chemistry and Physics
Open Access

Impact of cirrus clouds heterogeneities on top-of-atmosphere thermal infrared radiation

T. Fauchez[1], C. Cornet[1], F Szczap[2], P. Dubuisson[1], and T. Rosambert[2]

[1]Laboratoire d'Optique Atmosphérique, Université Lille 1, Villeneuve d'Ascq, France
[2]Laboratoire de Météorologie Physique, Université Blaise Pascal, Clermont Ferrand, France

Correspondence to: C. Cornet (celine.cornet@univ-lille1.fr)

Received: 24 August 2013 – Published in Atmos. Chem. Phys. Discuss.: 24 October 2013
Revised: 13 March 2014 – Accepted: 6 April 2014 – Published: 5 June 2014

Abstract. This paper presents a study of the impact of cirrus cloud heterogeneities on the thermal infrared brightness temperatures at the top of the atmosphere (TOA). Realistic 3-D cirri are generated by a cloud generator based on simplified thermodynamic and dynamic equations and on the control of invariant scale properties. The 3-D thermal infrared radiative transfer is simulated with a Monte Carlo model for three typical spectral bands in the infrared atmospheric window. Comparisons of TOA brightness temperatures resulting from 1-D and 3-D radiative transfer show significant differences for optically thick cirrus ($\tau > 0.3$ at 532 nm) and are mainly due to the plane-parallel approximation (PPA). At the spatial resolution of 1 km × 1 km, two principal parameters control the heterogeneity effects on brightness temperatures: i) the optical thickness standard deviation inside the observation pixel, ii) the brightness temperature contrast between the top of the cirrus and the clear-sky atmosphere. Furthermore, we show that the difference between 1-D and 3-D brightness temperatures increases with the zenith view angle from two to ten times between 0° and 60° due to the tilted independent pixel approximation (TIPA).

1 Introduction

Cirrus clouds cover 15 % to 40 % of the Earth's surface (Sassen et al., 2008). The temperature difference between the cloud top and the surface leads to a warming of the atmosphere by capturing a part of the infrared radiation emitted by the Earth's surface and atmosphere. By contrast, a part of the solar incident radiation is reflected to space because of the parasol effect, but this is generally slight for high clouds. Therefore, cirrus clouds lead to a positive radiative effect (e.g., a greenhouse effect) and their knowledge and evolution are crucial in the understanding of the Earth's radiative budget (Hartmann and Short, 1980; Ohring and Clapp, 1980; Stephens, 2005; Eguchi et al., 2007).

Global observations are well adapted to follow and better understand cloud evolution and characteristics. With this aim, many satellites are dedicated to cloud obervations from visible to microwave ranges. Algorithms usually used to retrieve cloud parameters from passive instruments, such as optical thickness and effective diameter of ice crystals, assume that clouds are homogeneous and infinite between two planes. This assumption is called the homogeneous independent pixel approximation (IPA; Cahalan et al., 1994) or independent column approximation (ICA; Stephens et al., 1991). However, real clouds can be far from this idealized model and this assumption may lead to biases in the retrieval of cloud properties.

In this context, radiative transfer modeling is very useful for studying the 1-D bias as a function of the cirrus structure and composition. Many studies have been conducted on the impact of cloud heterogeneities in the visible range and principally for warm clouds (Marshak and Davis, 2005). However, only few studies have been performed on cirrus cloud heterogeneities in the thermal infrared and they concern mainly fluxes or heating/cooling rates. Concerning fluxes, Hogan and Kew (2005) showed that radiative transfer calculations using IPA can change the mean The mean Top Of Atmosphere (TOA) radiative fluxes by about 45 W m^{-2} in the shortwave and 15 W m^{-2} in the long wave. Furthermore, Chen and Liou (2006) showed that significant impact exists on the broadband thermal cooling rates (around 10 %)

when the 3-D radiative transfer is compared to 1-D radiative transfer.

As far as we know, no study has been made concerning the heterogeneity bias on the infrared radiative quantities measured by space sensors. However, satellites, such as the Imaging Infrared Radiometer (IIR; Garnier et al., 2012, 2013) or the Moderate Resolution Imaging Spectroradiometer (MODIS; Cooper et al., 2007; Wang et al., 2011), use TOA brightness temperatures (BTs) or radiances in the thermal infrared window to retrieve cloud parameters. In this paper, we study the impact of cirrus heterogeneities in this spectral domain. In Sect. 2, we present the model 3DCloud (Szczap et al., 2014), used to generate realistic cloud scenes, and the Monte Carlo 3-D radiative transfer code named 3DMCPOL (Cornet et al., 2010), used to simulate the radiative transfer inside three dimensional (3-D) atmospheres. We simulate BTs for several cirri generated from realistic conditions as well as from measurements made during the CIRrus CLoud Experiment-II (CIRCLE II) airborne campaign (Mioche et al., 2010; Sourdeval et al., 2012). In Sect. 3, the biases due to heterogeneities are quantified by comparing the 3-D and 1-D BT at the IIR spatial resolution (1 km × 1 km). Summary and conclusions are given in Sect. 4.

2 Cirrus cloud generation

In order to simulate the impact of cirrus heterogeneities on the TOA BT, realistic 3-D cirri need to be generated. Firstly, 3-D cirrus ice water content (IWC) was simulated with a cloud generator based on basic atmospheric equations as well as Fourier transform framework to constrain invariant scale properties. Then, the optical properties are parametrized with two different models described hereafter.

2.1 3-D ice water content generation

Cirrus clouds are generated by the 3DCloud model (Szczap et al., 2014). First, basic atmospheric equations with idealized meteorological profiles are resolved in order to simulate the 3-D IWC. Then, scale invariant properties are constrained by the iterative Fourier framework. Hogan and Kew (2005) have shown that the IWC or 3-D extinction are characterized by a power spectrum with a $-5/3$ spectral slope. Generally, this spectral slope is delimited by a large scale limit L_{out} and a smaller scale limit corresponding to the cloud pixel spatial resolution. Hogan and Kew (2005) estimated from radar reflectivity and cirrus temperature that the IWC spectral slope is equal to $-5/3$ from scales of the order of a meter to a L_{out} of 50 km at the top of the cirrus, but it can decrease with the optical depth. Hogan and Kew (2005) have supposed that this decrease can be due to the coupled action of the wind shear with a spread of particle fall speeds leading to a homogenization of the IWC preferably at smaller scales. However, as we show later with lidar measurements, we do not observe a change in the spectral slope with the altitude (see the end of the section). Therefore, in our cirrus simulations, the spectral slope is assumed to be equal to $-5/3$ at all scales and altitudes.

Table 1. Cirri simulated by 3DCloud. "OP" corresponds to the optical properties parametrization, "CTA" corresponds to the cirrus top altitude, "Yal" represents the model of ice crystals developed by Yang et al. (2001, 2005) for aggregates ice crystals and "Bal" represents the parametrization of ice crystal optical properties developed by Baran et al. (2009); Baran (2012); Baran et al. (2013).

Cirrus	τ_c	ρ_τ	Deff (µm)	OP	CTA (km)
1	0.45	0.7	9.95	Yal	7.97
2	0.90	0.7	9.95	Yal	7.97
3	1.80	0.7	9.95	Yal	7.97
4	1.80	1.1	9.95	Yal	7.97
5	1.80	1.5	9.95	Yal	7.97
6	1.80	0.7	20.09	Yal	7.97
7	1.80	0.7	40.58	Yal	7.97
8	0.90	0.7	9.95	Yal	11.06
CII-1	0.41	0.77	variable	Bal	11.06
CII-2	0.81	0.77	variable	Bal	11.06
CII-3	0.90	0.70	9.95	Yal	11.06

For this study, two different cloud structures are generated. The first cirrus field (Fig. 1) is based on meteorological profiles to form a cirrus cloud as presented by Starr and Cox (1985), with the addition of a wind profile to form virgas. From this first realization, the influence on TOA BT of the cirrus mean optical thickness τ_c, the cirrus heterogeneity parameter ρ_τ, the ice crystal effective diameter D_{eff} and the cirrus altitude are easily tested. The heterogeneity parameter is defined by Szczap et al. (2000) as $\rho_\tau = \sigma_\tau/\tau_c$, with σ_τ being the standard deviation of the optical thickness. Eight cirri with different mean cloud parameters are generated (see Table 1). The cirrus mean optical thickness τ_c increases from 0.45 to 1.8, the cirrus heterogeneity parameter ρ_τ from 0.7 to 1.5, the ice crystal effective diameter D_{eff} from 9.95 µm to 40.58 µm and the altitude from 7.97 km to 11.06 km. These macrophysical parameters cover the characteristics of typical cirrus clouds (Sassen and Cho, 1992; Szczap et al., 2000; Carlin et al., 2002; Lynch et al., 2002), as well as the values of D_{eff}. Figure 1a shows an example of a 10 km × 10 km optical thickness field at 12.05 µm with a spatial resolution of 100 m and Fig. 1b the x-z view of the IWC.

The second cirrus is generated from measurements obtained on the 25 May 2007 during the CIRCLE II campaign (Mioche et al., 2010). CIRCLE II was an airborne campaign dedicated to the study of cirrus optical properties and the validation of space measurements made by the Cloud-Aerosol Lidar with Orthogonal Polarization (CALIOP; Winker et al., 2009) and the Infrared Imaging Radiometer (IIR; Garnier et al. (2012, 2013) on board Cloud-Aerosol Lidar and Infrared Pathfinder Satellite Observation (CALIPSO). This

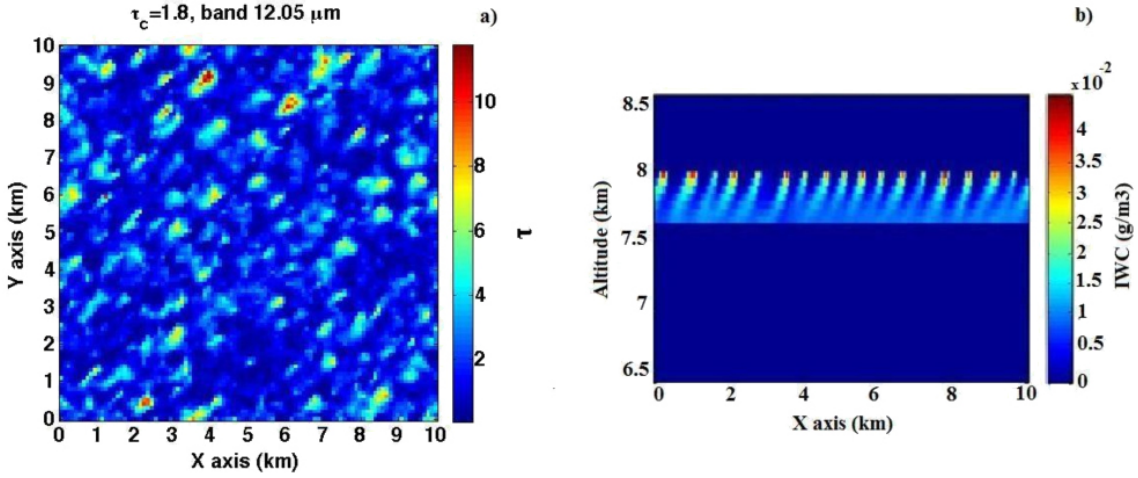

Figure 1. (a) 10 km × 10 km optical thickness field at 12.05 µm with a horizontal spatial resolution of 100 m; **(b)** x-z view of the cirrus ice water content (IWC) with a vertical spatial resolution of 58 m.

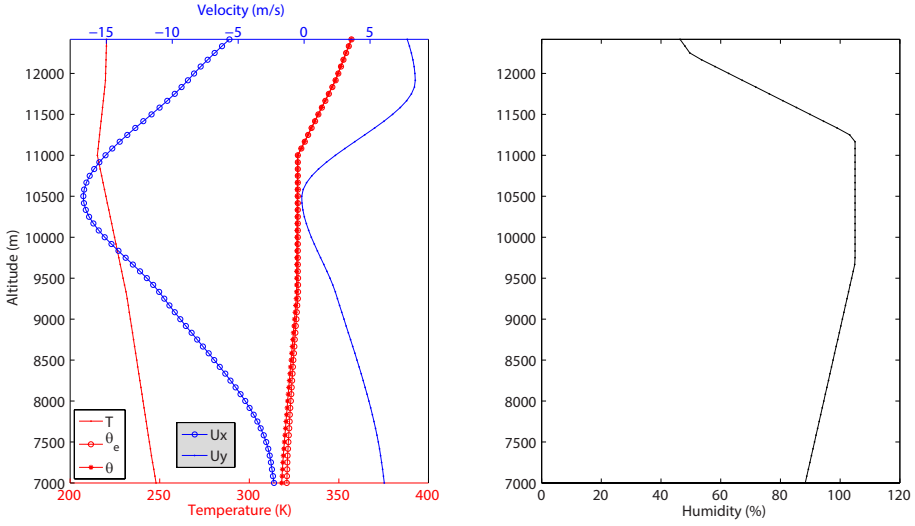

Figure 2. Basic state thermodynamic and moisture structure initially specified for cirrus CII-1 (with T being the thermodynamic temperature, θ the potential temperature, θ_e the equivalent potential temperature and Ux and Uy the wind profile on the x and y axes, respectively) and the relative humidity (%).

campaign consists of two Falcon 20 aircraft with several complementary onboard instruments to study cirrus cloud. In order to simulate the cirri observed during this campaign in a realistic way, we used the in situ measurements provided by the aircraft as well as IIR and MODIS (Moderate-Resolution Imaging Spectroradiometer; Platnick et al., 2003) radiometric measurements as input of 3DCloud. The cirrus mean IWC is determined by the combination of the CPI (cloud particle imager), more sensitive to small particles, and the PMS (particle measuring system) FSSP 300 probes, more sensitive to large particles. The extinction coefficient is obtained by the polar nephelometer (PN) and the cirrus mean optical thickness by IIR measurements. In addition, the meteorological profiles (wind speed and orientation, temperature, humidity, etc.) are set in the model (Fig. 2) using the meteorological data provided by the European Center for Medium-Range Weather Forecasts (ECMWF) with adaptations of the potential temperature and relative humidity profiles necessary to form cirri (Starr and Cox, 1985).

The scale-invariant properties are controlled by a $-5/3$ constant spectral slope at all the scales and altitude levels according to the cirrus backscattering coefficient at 532 nm measured at different altitudes by the lidar CALIOP/CALIPSO (Fig. 3), and the extinction coefficient measured by the polar nephelometer at the aircraft altitude.

To compare real measurements and 3DCloud simulations, the MODIS "true color Red Green Blue (RGB)" picture of the cirrus is presented in Fig. 4a. Figure 4b corresponds

Table 2. Optical parameters for aggregate ice crystals of the P. Yang model (Yang et al., 2001, 2005) used in cirrus 1 to 8 and CII-3.

D_{eff} (µm)	Band at 8.65 µm			Band at 10.60 µm			Band at 12.05 µm		
	σ_e	ϖ_0	g	σ_e	ϖ_0	g	σ_e	ϖ_0	g
9.95	1.704	0.771	0.879	0.951	0.317	0.880	1.716	0.410	0.860
20.09	2.460	0.748	0.938	1.480	0.439	0.961	1.951	0.471	0.925
40.58	2.054	0.603	0.944	1.838	0.499	0.979	1.966	0.494	0.944

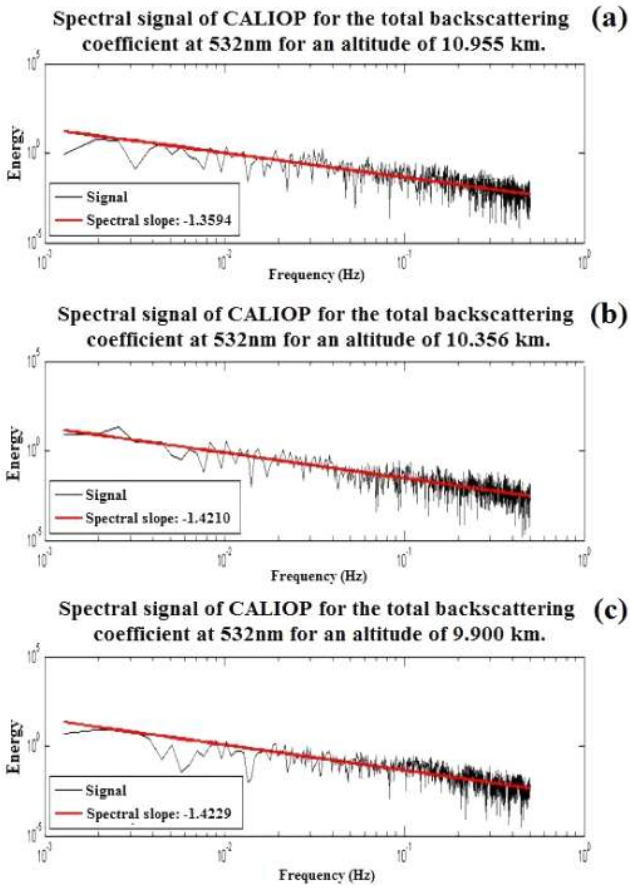

Figure 3. Spectral slopes of the CALIOP/CALIPSO backscattering coefficient at 532 nm observed at 10.955 km **(a)**, 10.356 km **(b)** and 9.900 km **(c)** as a function of the frequency in Hz .

to the CALIOP/CALIPSO vertical profile of the cirrus attenuated backscattering coefficient. Figure 4c represents the 20 km × 20 km optical thickness field at a spatial resolution of 100 m generated by 3DCloud inside the black rectangle of Fig. 4a, and 4d represents the IWC profile with a vertical resolution of 58 m. In Fig. 4a and c, the lines in the cirrus have the same orientation. It illustrates that the cirrus generated by 3DCloud and that one observed on 25 May, 2007, during the CIRCLE II campaign, have a similar geometry. The mean optical thickness is set to $\tau_c = 0.41$ in the model as is that retrieved from the IIR measurements in the black rectangle area. Furthermore, the comparison of Fig. 4b and d allows us to see that the vertical profiles of the simulated and observed cirri present the same cloud top and base altitudes. Three different simulations were done from the cirrus field observed during CIRCLE II and their properties are summarized in Table 1. Cirrus CII-1 corresponds to the simulation of the cirrus observed on 25 May. Cirrus CII-2 is the same but with the IWC increased twofold. Cirrus CII-3 has the same distribution of IWC but with optical properties of cirrus 8. Their properties are summarized in Table 1.

2.2 Cirrus optical property parametrization

Cirrus microphysical and optical properties are particularly difficult to apprehend because of the variability of shapes, sizes and orientations of ice crystals that can exist. Numerous studies have treated this problem and used different methods to compute the optical properties of cirrus clouds for visible and infrared wavelengths (Magono, 1966; C. Labonnote et al., 2000; Yang et al., 2001, 2005; Baum et al., 2005, 2011; Baran and Labonnote, 2007; Baran et al., 2009; Baran, 2012; Baran et al., 2013). Among all the available methods, we choose for cirrus 1 to 8 to use the ice crystals model developed by Yang et al. (2001, 2005). This model allows us to supply an extinction coefficient, a single scattering albedo and an asymmetry factor for seven forms of crystals having an effective diameter from 1 µm to 10, 000 µm. In our simulations, the aggregate shape with a monodisperse distribution is selected because it is one of those used in the IIR retrieval algorithm (Garnier et al., 2013). Furthermore, in the thermal infrared, the forward peak is weak and the particle phase functions are smooth enough to be approximated by the Henyey–Greenstein phase function (Henyey and Greenstein, 1940) and this is assumed in the Yang et al. (2001, 2005) model. Values of the extinction coefficient efficiency, the single scattering albedo and the asymmetry parameter are presented in Table 2.

The model of Yang et al. (2001, 2005) based on the effective diameter does not allows us to represent its three-dimensional variability in the cirrus. To study the impact of the optical property variabilities on the TOA BT, we use the parametrization developed by Baran (2012) and Baran et al. (2013) for the CII-1 and CII-2 cirrus. Baran et al. (2009) show that the extinction coefficient σ_e, the single scattering albedo ϖ_0 and the asymmetry factor g could be related to the

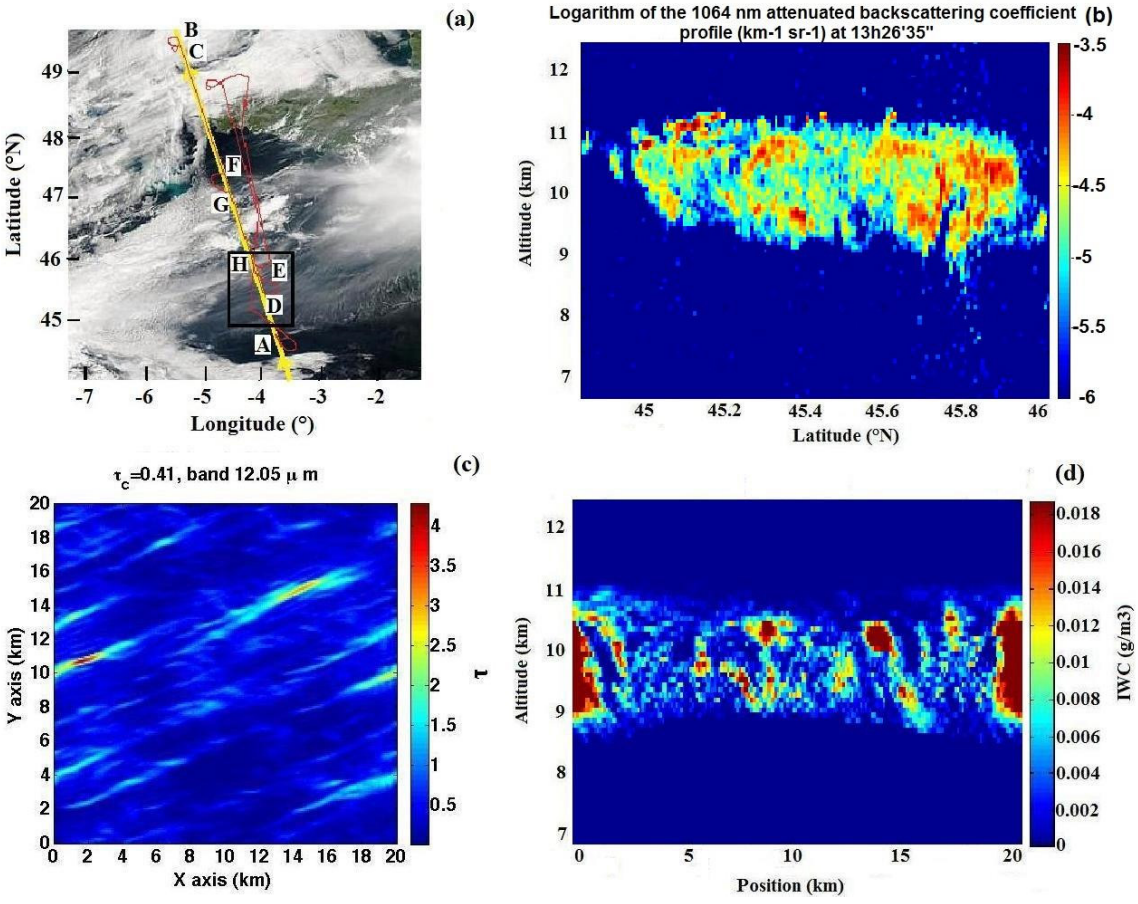

Figure 4. Observed ((**a**), (**b**)) and simulated ((**c**), (**d**)) cirrus cloud on 25 May, 2007 during the CIRCLE II campaign. **(a)** shows the MODIS "true color RGB" picture of the cirrus. The bold yellow line represents the CALIOP track and the red line the French Falcon 20 flight. Measurements start from point A to finish at point H. The black rectangle represents the cirrus area without any low-water cloud below. **(b)** represents the vertical profile of the attenuated backscattering coefficient of the cirrus observed by the lidar CALIOP/CALIPSO inside the black rectangle in **(a)**. **(c)** represents the 20 km × 20 km optical thickness field generated at 12.05 µm with a horizontal spatial resolution of 100 m and with the mean optical thickness $\tau_c = 0.41$ observed by IIR at 12.05 µm. **(d)** represents the x-z view of the cirrus IWC generated by 3DCloud with a vertical resolution of 58 m.

couple (IWC, Temperature). The relations between optical properties and the couple (IWC, Temperature) were obtained from more than 20 000 particle size distributions (PSD) provided by in situ measurements (Field et al., 2005, 2007). Therefore, from a realistic 3-D profile of IWC and temperature, we employed this parametrization to generate the 3-D heterogeneous optical property field for the CII-1 and CII-2 cirrus. Their vertical optical property distributions are presented in Fig. 5. The corresponding vertical temperature profile is shown in Fig. 2 and the IWC vertical profile in Fig. 4d.

2.3 Radiative transfer modeling

Thermal radiative transfer computations are made with the 3-D Monte Carlo code, 3DMCPOL, initially developed in the visible range by Cornet et al. (2010) and extended for this study to the thermal infrared (TIR). In 3DMCPOL, the atmosphere is divided into voxels (3-D pixels), with a constant horizontal size (*dx*, *dy*) and a variable vertical size *dz*. Each of the voxels is described by the cloud optical properties: the extinction coefficient σ_e, the single scattering albedo ϖ_0, the phase function and the cloud temperature T_c. 3DMCPOL is a forward Monte Carlo which used the local estimate method (LEM; Marshak and Davis, 2005; Mayer, 2009). It was first developed for the visible range where the initial direction of photon packages is given by the solar direction. The extension of the code to the TIR conserved the forward method, even if the source of emission can be the atmosphere, the surface or the cloud.

Monte Carlo methods consist in following photon packages, which undergo some scattering and absorption processes in the atmosphere and surface reflections. At each scattering event, the LEM is used and consists of computing the contribution of emission, scattering or reflection events

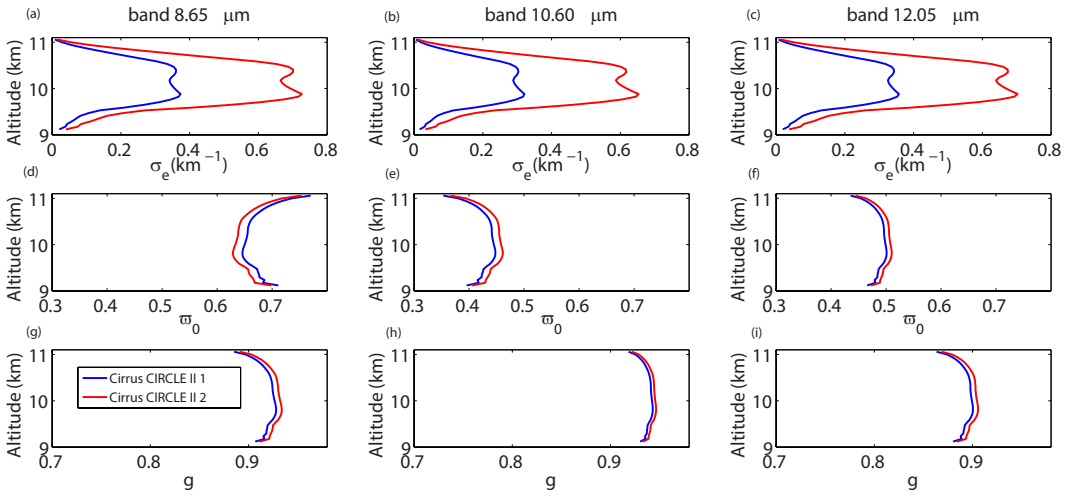

Figure 5. **(a)**, **(b)** and **(c)**: vertical variation of the mean extinction coefficient σ_e; **(d)**, **(e)** and **(f)**: vertical variation of the single scattering albedo ϖ_0; and **(g)**, **(h)** and **(i)**: vertical variation of the asymmetry factor g for the three channels at 8.65 µm, 10.60 µm and 12.05 µm and for the cirrus CII-1 (blue curves) and CII-2 (red curves).

into the detector direction, attenuated by the medium optical thickness between the place of interaction and the detector. The LEM weight W_{le} attached to the photon is thus defined as

$$W_{le} = \frac{W_{\varpi_0} P_{11}(\theta_s) \exp(-\tau_m)}{\cos(\theta_v)}, \quad (1)$$

with P_{11} being the first element of the scattering matrix which gives the probability of a photon being scattered in the direction of the detector, θ_s the scattering angle between photon direction and the detector, τ_m the medium optical thickness from the interaction to the detector and θ_v the zenith view angle. W_{ϖ_0} is the weight due to the cloud absorption and it corresponds at each interaction to the product of the single scattering albedo ϖ_0 for cloud scattering (or of the surface albedo α for surface reflection). When W_{ϖ_0} is less than 10^{-6}, the contribution of the photon package is considered to be negligible and a new one is launched.

To include the gaseous absorption in 3DMCPOL, we use the correlated k-distribution method (Lacis and Oinas, 1991; Kratz, 1995). This technique allows us to take into account the absorption variations in each spectral band by dividing the range of absorption coefficient values into bins using a sum of weighted exponentials. To each bin, a weight a_{ib} is assigned whose sum is equal to 1. However, to avoid running radiative transfer for every bin, which is very time consuming, we use the equivalence theorem (Partain et al., 2000; Emde et al., 2011). It consists of attaching an absorption vector $\boldsymbol{W}_g$ to the photon package, with a size corresponding to the bin number nbin of the correlated k-distribution. $\boldsymbol{W}_g(ib)$ is expressed by Eq. (2).

$$\boldsymbol{W}_g(ib) = \exp\left(-\int_0^l k_g(ib, z) dl'\right), \quad (2)$$

with ib being the number of the correlated k-distribution bin, l the photon package path and $k_g(ib, z)$ the absorption coefficient for bin ib and altitude z.

With the gaseous absorption, the LEM weight W_{le} becomes a vector of size nbin as follows:

$$\boldsymbol{W}_{le}(ib) = \frac{W_g(ib) W_{\varpi_0} P_{11}(\theta_s) \exp(-\tau_m)}{\cos(\theta_v)}. \quad (3)$$

With this method, it is possible to compute the reflectance for a spectral band with variable gaseous absorption with one Monte Carlo radiative transfer (RT) simulation, as long as the medium optical properties are homogeneous. The other important modification concerns the sources of emission. The total number of emission processes (or photon packages) is fixed in the input by the user and a fraction of the total number of photon packages corresponds to each source (cloud, surface and gases). This fraction is obtained as a function of the emission characteristics (emissivity, temperature) of all the corresponding voxels. We compute a quantity called the source flux F, defined as the energy emitted in every direction by each cell of the emission source. As emission processes are isotropic, the direction of emission is chosen randomly. The sum of the source flux of the cloud, the surface and the gases ($F_c + F_s + F_g$, respectively) over all the cells gives the total emitted energy. The number of photons emitted by a source type is then the proportion of energy of this source to the total energy. A random choice determines the spatial location where the emission takes place.

The source flux F is computed from the radiance R. For cloud cell, the source flux F_c is defined as

$$F_c = 4\pi\ R_c = 4\pi\ \tau_a\ B(T_c) = 4\pi\ (1 - \varpi_0)\ \tau_e\ B(T_c), \quad (4)$$

with R_c being the cloud radiance emitted by the cell, τ_a and τ_e the absorption and extinction optical thicknesses, respectively, $B(T_c)$ the Planck function at the temperature T_c and

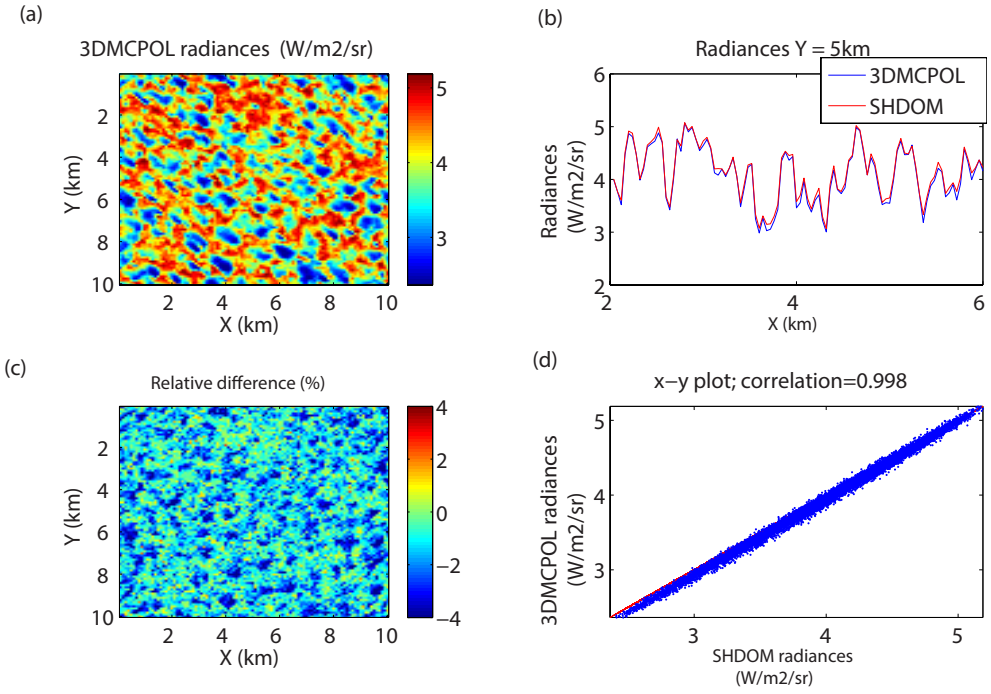

Figure 6. Comparisons of 3DMCPOL and SHDOM radiance simulations at 10.60 µm for $\varpi_0 = 0.5$, $\tau_c = 1.8$ and for $\theta_v = \phi_v = 0°$. **(a)** 3DMCPOL TOA radiance field simulation at the nadir; **(b)** 3DMCPOL and SHDOM radiances along the x axis for Y = 5 km; **(c)** relative differences $(3DMCPOL - SHDOM/3DMCPOL) \times 100\,(\%)$ between 3DMCPOL and SHDOM radiances; **(d)** 3DMCPOL-SHDOM correlation plot.

ϖ_0 the single scattering albedo. In the same way, the source flux F_s emitted from the surface is defined as

$$F_s = \pi\ R_s(\theta, \phi) = \pi\ \epsilon_s\ B(T_s), \tag{5}$$

with R_s, ϵ_s and T_s being the surface radiance, the emissivity and the surface temperature, respectively. Finally, the source flux F_g emitted by the gases as a function of bin ib is expressed by

$$F_g(ib) = 4\pi\ R_g(ib) = 4\pi\ a_{ib}\ \tau_g(ib) B(T_c), \tag{6}$$

with a_i being the weight associated to bin ib and $\tau_g(ib)$ the gaseous optical thickness.

Validation of the 3DMCPOL modifications was done by intercomparisons with Spherical Harmonic Discrete Ordinate Method (SHDOM) simulations (Evans, 1998). An example of a comparison between 3DMCPOL and SHDOM is illustrated in Fig. 6 at the scale of 100 m × 100 m for cirrus 3 and for $\theta_v = \phi_v = 0°$. Three and half billion photon packages were launched, which lead to a statistical accuracy of about $10^{-3} W.m^{-2}.sr^{-1}$. Figure 6a shows the 3DMCPOL radiance field of view at the nadir, Fig. 6b presents the comparison of 3DMCPOL and SHDOM radiances along the x axis for Y = 5 km, Fig. 6c shows the relative difference (%) field between 3DMCPOL and SHDOM radiances and Fig. 6d represents the correlation plot between 3DMCPOL and SHDOM radiances. The relative error between 3DMCPOL and SHDOM simulations is generally under 2% and the correlation between the two models is 0.998. The small remaining differences can be explained by the different treatment of the medium properties, as 3DMCPOL considers the medium properties homogeneous in each voxel while SHDOM interpolates the properties in a voxel. Comparisons were also been made for several cases of cirrus, with a different geometry of observation ($\theta_v = 30°$,60° and $\phi_v = 45°$, 90°, 180°) and spectral bands (at 8.65 µm and 12.05 µm), and gave similar results.

3 Heterogeneity effects on the brightness temperatures simulated at TOA

3.1 Description of the heterogeneity effects

Clouds present many variabilities at different scales. In retrieval algorithms, for simplification and for computational reasons, the independent column approximation (ICA; Stephens et al., 1991) is commonly applied: cloud layers are assumed to be vertically and horizontally homogeneous, independent of each other with an infinite horizontal extent. At the scale of IIR (or MODIS) observation pixel (1 km × 1 km), the radiative transfer is supposed to be 1-D without horizontal transport between columns. To study cirrus heterogeneities that can affect BT observed in the thermal infrared at TOA, we made 3-D and 1-D simulations with 3DMCPOL. 3-D BT are simulated at the

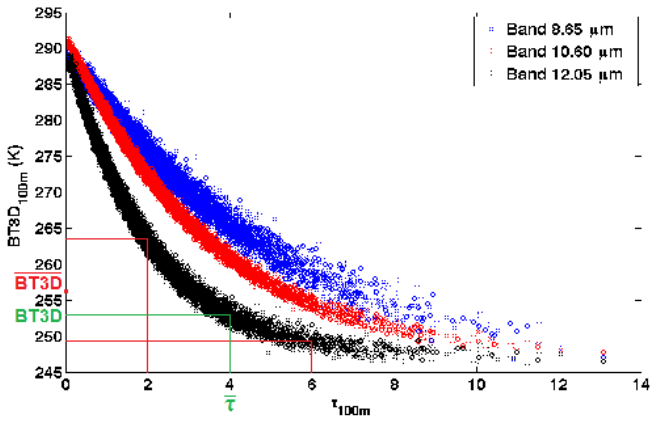

Figure 7. Variation of the 3-D brightness temperatures $BT3D_{100\,m}$ as a function of the optical thickness at $100\,m \times 100\,m$ $\tau_{100\,m}$ for the three IIR channels and for cirrus 5. $\overline{BT3D}$ represents the average of $BT3D_{100\,m}$, corresponding to two $\tau_{100\,m}$, $BT3D$ represents the 3-D brightness temperature corresponding to the mean optical thickness $\bar{\tau}$. The mathematical formulation of the PPA due to the Jensen inequality is expressed by $\overline{BT3D} > BT3D(\bar{\tau})$.

spatial resolution of $100\,m \times 100\,m$ and then averaged to $1\,km \times 1\,km$ ($BT3D_{1\,km}$). For 1-D BT, cloud properties are first averaged at $1\,km \times 1\,km$ before simulating BT ($BT1\text{-}D_{1\,km}$). Note that the spatial resolution is an important parameter in the study of the impact of cirrus heterogeneities on BT and our results are, thus, only applicable for a spatial resolution close to $1\,km \times 1\,km$.

To describe the heterogeneity effects, in Fig. 7 we plot the BT at 100 m ($BT3D_{100\,m}$) as a function of the optical thickness at 100 m ($\tau_{100\,m}$) for cirrus 5 and for the three IIR channels (8.65 µm, 10.60 µm and 12.05 µm). We see that the relation is nonlinear and the averaging of BT leads to Jensen inequality, usually called the plane-parallel approximation (PPA). The width of the $BT3D_{100\,m}$ distribution, which is about 4–5 K, is due, on the one hand, to the vertical variability of the extinction coefficient and, on the other hand, to the photon horizontal transport between cloud columns (Varnai and Marshak, 2001). The PPA thus causes the average of BT ($\overline{BT3D}$) to be higher than the BT of the average of optical thicknesses $\bar{\tau}$.

In Figs. 8 and 10, we plot the absolute value of the BT differences at the scale of 100 m ($|\Delta BT_{100\,m}|$), and 1 km, ($|\Delta BT_{1\,km}|$), respectively, for a case of a very inhomogeneous cirrus (cirrus 5). We plot for brightness temperatures, but results are similar in radiance space. Note that, for 3-D brightness temperatures at $100\,m \times 100\,m$ ($BT3D_{100\,m}$), the extinction coefficient varies vertically, but not for the 1-D brightness temperatures at $100\,m \times 100\,m$ ($BT1\text{-}D_{100\,m}$). Several effects contribute to the differences between 3-D and 1-D BT and are described below for the 100 m spatial resolution (Fig. 8):

- We plot the absolute value of the extinction vertical heterogeneity effect $|BT1 - Dvhe_{100\,m} - BT1 - D_{100\,m}|$ in green, with $BT1 - Dvhe_{100\,m}$ corresponding to 1-D radiative transfer with independent column and vertically heterogeneous extinction coefficient.

- We plot the absolute value of the BT difference due to the horizontal transport which is computed with the calculation of $|BT3Dvho_{100\,m} - BT1 - D_{100\,m}|$ in red, with $BT3Dvho_{100\,m}$ corresponding to 3-D radiative transfer with vertically homogeneous extinction.

- We plot the absolute value of the difference $|\Delta BT_{100\,m}|$ obtained with the calculation of $|BT3D_{100\,m} - BT1 - D_{100\,m}|$ in blue. Note that $|\Delta BT_{100\,m}|$ is not the sum of the two effects described above because some of them can be opposing.

In addition, we also plot the absolute value of the statistical error (black line) due to the statistical approach of the Monte Carlo algorithm, which is about 0.5 K.

We see that at 100 m the $|\Delta BT_{100\,m}|$ for the band at 8.65 µm is larger and dominated by the horizontal transport effect because the scattering is greater for this band than for the two others. By contrast, the vertical extinction variability, which is also associated to the vertical emissivity variability, is larger at 10.60 µm and at 12.05 µm than for the band at 8.65 µm. For these two bands, the horizontal transport effect and the vertical extinction variability are of the same order and thus contribute with equal prominence to the total differences $|\Delta BT_{100\,m}|$. The results are similar for the other cirrus cases and they are not presented here.

To evaluate the horizontal photon transport effects on TOA BT, we present a step cirrus cloud in Fig. 9. The optical thickness described at the scale of 100 m ($\tau_{100\,m}$) is equal to 3.5 between 0 km and 2 km and to 0 after that. "Thin cirrus" (solid lines) and "thick cirrus" (dashed lines) are two cirri with the same optical thickness and the same top altitude but with different geometrical thickness (0.4 km and 2 km, respectively). Curves represent the 3-D brightness temperatures whereas the straight lines correspond to 1-D brightness temperatures computed using the IPA assumption. Logically, pixels with optical thickness equal to zero have large BTs corresponding to clear-sky atmosphere, while pixels with larger optical thickness have lower BTs corresponding to the top of the cirrus. Due to the stronger absorption at 12.05 µm, the BT differences between opaque pixels and clear-sky pixels are greater for the band at 12.05 µm than at 8.65 µm. We note also that BTs of "thick cirri" are larger than those of "thin cirri" because for the "thick cirrus", the energy emitted by the cloud base, which is closer to the surface, is greater. Photon horizontal transport effects are visible near the optical thickness transition (between $\tau_{100\,m} = 0$ and 3.5), where photons emitted from the surface cross over or are scattered in the cloud leading to an increase in the BT. This increase goes

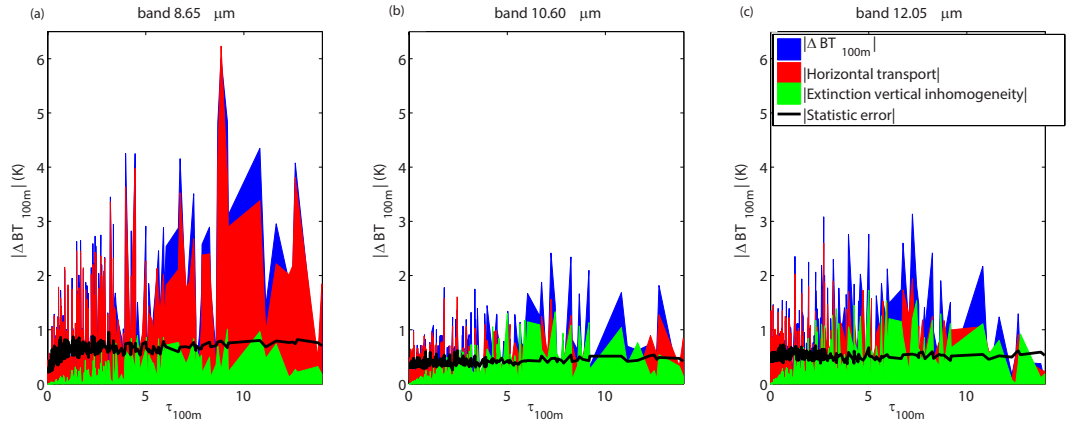

Figure 8. Absolute brightness temperature differences at 100 m × 100 m $\Delta BT_{100\,\mathrm{m}}$ (in blue) due to the horizontal transport (in red), the extinction vertical variability (in green) and the statistical error of the code (black line) for cirrus 5. Results are presented for the bands at 8.65 µm, 10.60 µm and 12.05 µm.

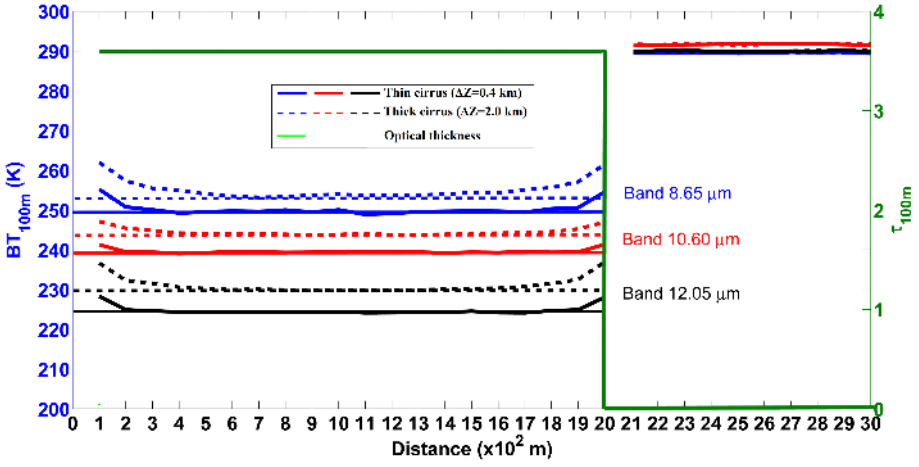

Figure 9. Brightness temperatures at the scale of 100 m ($BT_{100\,\mathrm{m}}$) as a function of the distance from the left cloud edge for a step cirrus cloud. The bold green line corresponds to the optical thickness at the scale of 100 m ($\tau_{100\,\mathrm{m}}$); straight lines correspond to 1-D brightness temperatures and curves to 3-D brightness temperatures. Bold lines refer to brightness temperatures of the geometrically thin cirrus ($\Delta Z = 0.4$ km) and dashed lines to the geometrically thick cirrus ($\Delta Z = 2.0$ km); blue, red and black colors correspond to 8.65 µm, 10.60 µm and 12.05 µm, respectively.

further in the case of the "thick cirrus" because the mean extinction coefficient per cell is smaller and photons can spread further. For bands at 10.60 µm and at 12.05 µm, with larger absorption, cloud pixels are impacted until 100 m for "thin cirri "and 400–500 m for "thick cirri". At 8.65 µm, cloud pixels up to 1 km from the cloud edge can be impacted. We note that, based on the IIR accuracy of 1 K, photon horizontal transport effects become, on average, larger than this accuracy below a spatial resolution of 250 m.

At the scale of 1 km × 1 km (Fig. 10) the horizontal transport (red) and the extinction vertical heterogeneity (green) effects are slight. This means that the absolute difference $|\Delta BT_{1\,\mathrm{km}}|$ (blue) between $BT3D_{1\,\mathrm{km}}$ and $BT1 - D_{1\,\mathrm{km}}$ is strongly dominated by the PPA. It reaches more than 12 K for the largest optical thicknesses in the three bands. Horizontal transport in the band at 8.65 µm is larger than in the other bands, but remains low compared to the total difference $|\Delta BT_{1\,\mathrm{km}}|$. The extinction vertical inhomogeneity also appears to be negligible at the 1 km × 1 km scale. In summary, Fig. 10 shows that, at the scale of IIR and MODIS, the most important difference between $BT3D_{1\,\mathrm{km}}$ and $BT1 - D_{1\,\mathrm{km}}$ is due to the PPA. During the retrieval process, the cloud properties retrieved from brightness temperatures at the 1 km × 1 km pixel will thus be different from the mean cloud properties.

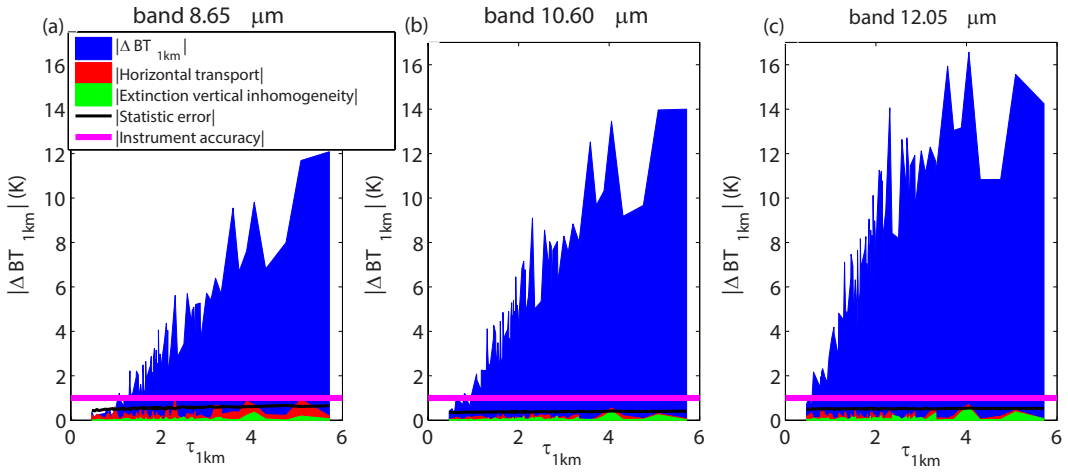

Figure 10. Absolute brightness temperature differences at 1 km × 1 km $\Delta BT_{1\,\mathrm{km}}$ (in blue) due to the horizontal transport (in red), the extinction vertical variability (in green), the statistical error of the code (black line) and the IIR instrumental accuracy (pink line) for cirrus 5. Results are presented for the bands at 8.65 µm, 10.60 µm and 12.05 µm.

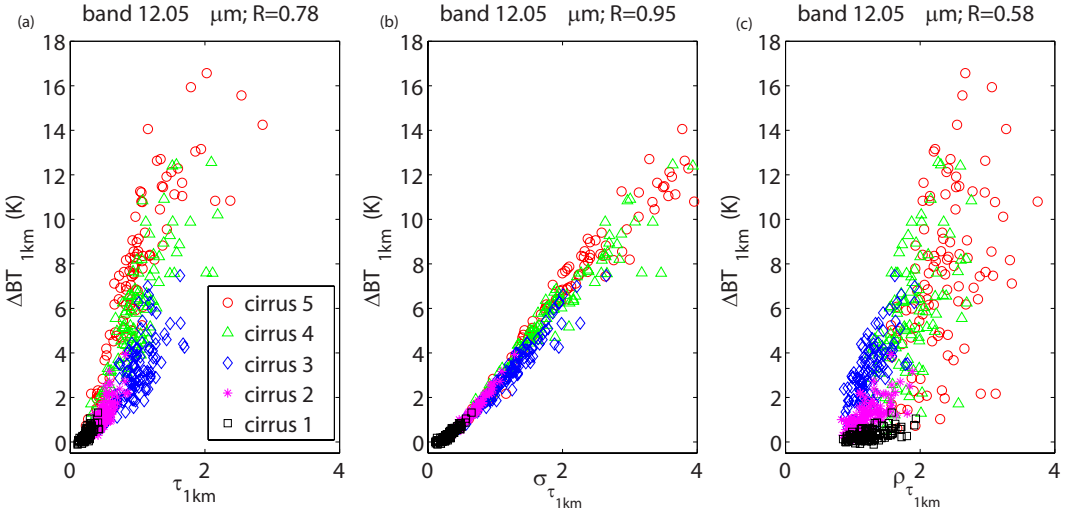

Figure 11. Brightness temperature differences, $\Delta BT_{1\,\mathrm{km}}$, as a function of the optical thickness $\tau_{1\,\mathrm{km}}$, the optical thickness standard deviation $\sigma_{\tau_{1\,\mathrm{km}}}$ and the heterogeneity parameter $\rho_{\tau_{1\,\mathrm{km}}}$ for different cirri presented Table 1 and for the band at 12.05 µm. R represents the correlation coefficient computed for the five cirri.

3.2 Heterogeneity effects due to optical thickness variabilities

This section focuses on the impact of the optical thickness variabilities on TOA BT, all the other parameters being constant (atmospheric profile, altitude, geometrical thickness, surface temperature, particles size and shape). Figure 11 presents the heterogeneity effects on the brightness temperatures ($\Delta BT_{1\,\mathrm{km}}$) for the band at 12.05 µm as a function of the optical thickness $\tau_{1\,\mathrm{km}}$ (Fig. 11a), the standard deviation of the optical thickness $\sigma_{\tau_{1\,\mathrm{km}}}$ computed from the 100 pixels of 100 m × 100 m (Fig. 11b), and the heterogeneity parameter $\rho_{\tau_{1\,\mathrm{km}}}$ at 1 km × 1 km (Fig. 11c). We see that the difference $\Delta BT_{1\,\mathrm{km}}$ is better correlated with $\sigma_{\tau_{1\,\mathrm{km}}}$ (R=0.95). Indeed, as discussed previously, the PPA is the most important effect at this scale. We notice that the larger $\sigma_{\tau_{1\,\mathrm{km}}}$ is, the greater $\Delta BT_{1\,\mathrm{km}}$ is. Furthermore, as the increase in $\tau_{1\,\mathrm{km}}$ is not totally correlated with the increase in $\sigma_{\tau_{1\,\mathrm{km}}}$, the correlation between $\Delta BT_{1\,\mathrm{km}}$ and $\tau_{1\,\mathrm{km}}$ is smaller, as is the correlation between $\Delta BT_{1\,\mathrm{km}}$ and $\rho\tau_{1\,\mathrm{km}}$. The $\sigma_{\tau_{1\,\mathrm{km}}}$ appears, therefore, to be the best parameter to highlight the heterogeneity effects and it will be used below to represent the field heterogeneity.

The $\Delta BT_{1\,\mathrm{km}}$ as a function of the standard deviation $\sigma_{\tau_{1\,\mathrm{km}}}$ for the different cirri of Table 1 and for the three channels of the IIR is presented in Fig. 12. The first remark on this figure is that the correlation coefficient R is better than 0.80 for all the cirri, except for cirrus 1. For this cirrus, the lowest optical thickness (0.45) associated with the strong scattering

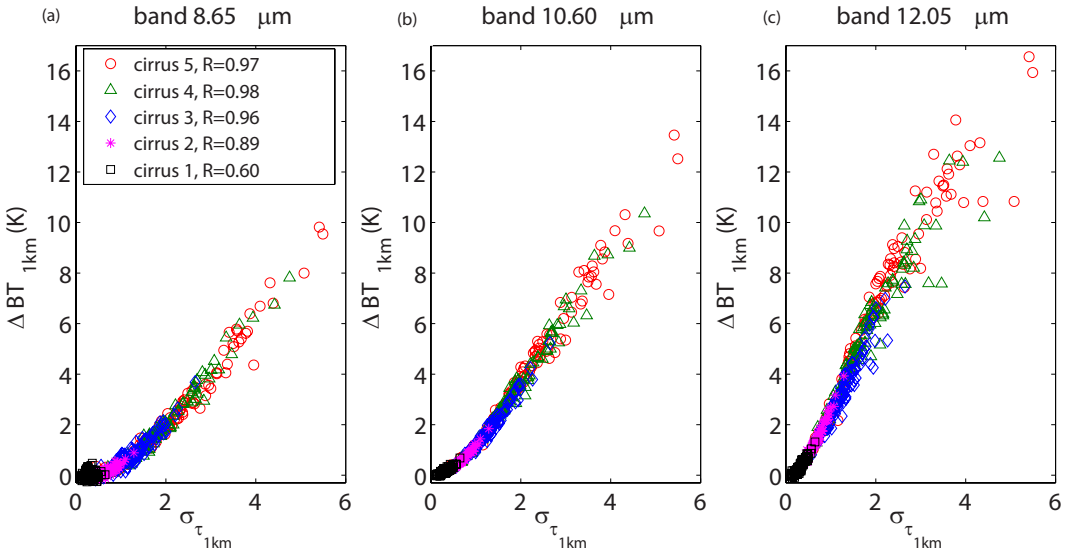

Figure 12. Brightness temperature differences, $\Delta BT_{1\,\mathrm{km}}$, viewed at the nadir as a function of the optical thickness standard deviation $\sigma_{\tau_{1\,\mathrm{km}}}$ for different cirri presented in Table 1. R represents the average correlation coefficient over the three bands.

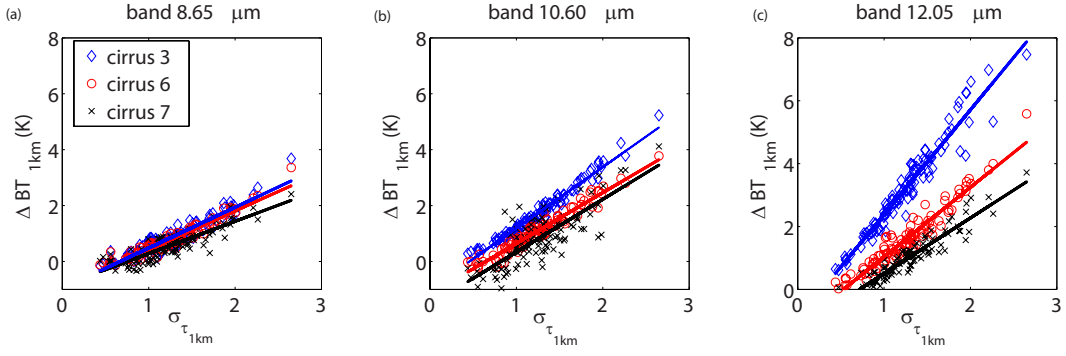

Figure 13. Brightness temperature differences, $\Delta BT_{1\,\mathrm{km}}$, viewed at the nadir as a function of the optical thickness standard deviation $\sigma_{\tau_{1\,\mathrm{km}}}$ for the same three cirrus fields with different ice crystal effective diameters: cirrus 3 ($D_{\mathrm{eff}} = 9.95\,\mu\mathrm{m}$), cirrus 6 ($D_{\mathrm{eff}} = 20.09\,\mu\mathrm{m}$) and cirrus 7 ($D_{\mathrm{eff}} = 40.58\,\mu\mathrm{m}$).

at 8.65 µm lead to smoothing of the variability due to the photon horizontal transport. The five cirri have similar characteristics with different mean optical thickness τ_c and heterogeneity parameter ρ_τ. For each of them, $BT3D_{1\,\mathrm{km}}$ and $BT1 - D_{1\,\mathrm{km}}$ are computed for 100 pixels of 1 km × 1 km. We see that the relation between $\Delta BT_{1\,\mathrm{km}}$ and $\sigma_{\tau_{1\,\mathrm{km}}}$ is almost linear for the pixels presented in this study that are for optical thicknesses below 2. This figure shows that, for the same altitude, geometrical thickness and optical properties, $\Delta BT_{1\,\mathrm{km}}$ depends mainly on the optical thickness sub-pixel heterogeneity, the optical thickness sub-pixel distribution being almost insignificant. Note that, similar results were obtained in the visible (Szczap et al., 2000; Cornet et al., 2004) where heterogeneity effects depend mainly on $\tau_{1\,\mathrm{km}}$ and $\sigma_{\tau_{1\,\mathrm{km}}}$.

We now study the impact of optical thickness heterogeneities for different ice crystal effective diameters D_{eff}. In Fig. 13, we present $\Delta BT_{1\,\mathrm{km}}$ as a function of $\sigma_{\tau_{1\,\mathrm{km}}}$ for $D_{\mathrm{eff}} = 9.95\,\mu\mathrm{m}$, $20.09\,\mu\mathrm{m}$ and $40.58\,\mu\mathrm{m}$. The crystal model used is the P. Yang model (Yang et al., 2001, 2005; Table 2) for an aggregate shape. This figure shows that $\Delta BT_{1\,\mathrm{km}}$'s decrease with the increase in D_{eff} for the three TIR bands. For the bands at 10.60 µm (Fig. 13b) and at 12.05 µm (Fig. 13c), the single scattering albedo ϖ_0 and the asymmetry parameter g increase with D_{eff} (Table 2); this leads to a decrease in the absorption inside each 1 km × 1 km pixel and an increase in energy in the forward peak. Therefore, photons emitted from the surface cross the cloud more easily, leading to a decrease in the contrast between large and weak optical thicknesses. The radiative field heterogeneities thus appear smoothed. Concerning the band at 8.65 µm, ϖ_0 decreases with D_{eff} but the asymmetry parameter g increases. Between $D_{\mathrm{eff}} = 9.95\,\mu\mathrm{m}$ and $D_{\mathrm{eff}} = 20.09\,\mu\mathrm{m}$, the increase in g dominates and, as previously explained, the $\Delta BT_{1\,\mathrm{km}}$'s decrease. But between $D_{\mathrm{eff}} = 20.09\,\mu\mathrm{m}$ and $D_{\mathrm{eff}} = 40.58\,\mu\mathrm{m}$,

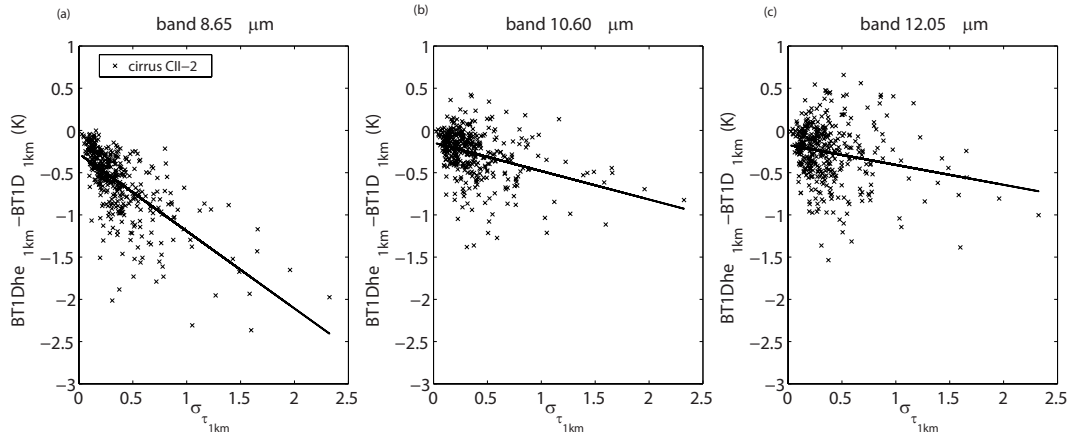

Figure 14. Differences between brightness temperatures viewed at the nadir between a 1-D radiative transfer with vertically heterogeneous columns ($BT1 - Dhe_{1\,\mathrm{km}}$) and with homogeneous columns ($BT1 - D_{1\,\mathrm{km}}$) as a function of the optical thickness standard deviation $\sigma_{\tau_{1\,\mathrm{km}}}$ for cirrus CII-2 and for the bands at 8.65 µm, 10.60 µm and 12.05 µm.

g increases slightly and ϖ_0 decreases. These two effects are opposite and the $\Delta BT_{1\,\mathrm{km}}$'s do not change significantly between these two effective sizes.

In summary, the amplitude of the optical thickness heterogeneity effect depends on the particle effective size when a constant size is supposed in the cloud. Indeed, in this situation, the optical properties can be very different from one crystal size to another and, thus, lead to different values. For example, the mean value of $\Delta BT_{1\,\mathrm{km}}$ for cirrus 3 is 3.12 K (band at 12.05 µm), while for cirrus 7 the mean value is 0.99 K. However, a unique crystal size and shape as supposed in these simulations is not realistic. It just allows us to obtain information on the influence of the crystal size on TOA BT. In reality, a large variety of particle sizes and shapes are present in cirri and, therefore, a more complex parametrization of the optical properties is necessary to study the impact of the optical property variabilities on TOA BT.

3.3 Heterogeneity effects due to optical and microphysical property variabilities

To study the effects of three-dimensional optical property heterogeneities on TOA BT and simulate more realistic clouds, we employed the parametrization developed by Baran et al. (2009); Baran (2012); Baran et al. (2013) (see Sect. 2.2). The cirri simulated from the CIRCLE II campaign are used to generate a heterogeneous macrophysical field (Fig. 4 and Table 1) and optical property field (Fig. 5). Note that the Field et al. (2007) parametrization is based on bulk measurements inside the cirrus and is not directly related to the cloud edges, where measurements can be different. However, as we showed, the microphysical properties have a slight influence on TOA brightness temperatures with regard to the IIR instrumental accuracy.

Before studying the heterogeneity effects, we look at the effects of vertical variabilities of the extinction coefficient σ_e, the single scattering albedo ϖ_0 and the asymmetry factor g (Fig. 14). The 1-D RT with homogeneous columns ($BT1 - D_{1\,\mathrm{km}}$) is compared with the 1-D RT with heterogeneous columns ($BT1 - Dhe_{1\,\mathrm{km}}$) for the CII-2 cirrus. We see that the difference is, on average, lower than 0.5 K for the three channels and it is a maximum for the band at 8.65 µm. Indeed, because the scattering is greater in this band and thus the absorption weaker, the vertical optical property variabilities have, therefore, a more significant impact on BT.

$\Delta BT_{1\,\mathrm{km}}$'s as a function of $\sigma_{\tau_{1\,\mathrm{km}}}$ are presented in Fig. 15 in the three IIR channels for the CII-1 and CII-2 cirrus with variable optical properties and for cirrus CII-3 with homogeneous optical properties. This last cirrus has been generated in order to compare, on the one hand, the two optical property models and, on the other hand, the influence of the cirrus vertical extension (see Sect. 3.4). In this figure, the mean correlation coefficient R averaged over the three channels between $\Delta BT_{1\,\mathrm{km}}$ and $\sigma_{\tau_{1\,\mathrm{km}}}$ is larger again than 0.80. The low value of R (0.88) for cirrus CII-1 is due to the band at 8.65 µm. Indeed, in this case, the PPA bias is close to zero, firstly because the $\sigma_{\tau_{1\,\mathrm{km}}}$ values are quite small and, secondly, because there is more scattering which tends to smooth the field heterogeneity and, thus, decorrelates the relation between $\Delta BT_{1\,\mathrm{km}}$ and $\sigma_{\tau_{1\,\mathrm{km}}}$. For this cirrus, which is the result of the realistic simulation obtained from the cirrus observed during the CIRCLE II campaign, the heterogeneity effects on the TOA BT are, on average, lower than the IIR instrumental accuracy (1 K). The PPA and IPA bias have, thus, a limited impact in this case. Concerning cirrus CII-3 with homogeneous optical properties, the $\Delta BT_{1\,\mathrm{km}}$ is slighter than for other cirri at 8.65 µm, but this difference decreases for the band at 10.60 µm and becomes positive for the band at 12.05 µm. Indeed, cirrus CII-3 contains only small aggregate crystals ($D_{\mathrm{eff}} = 9.95$ µm). As explained in Sect. 3.2, the PPA is larger for the band at 12.05 µm because small particles

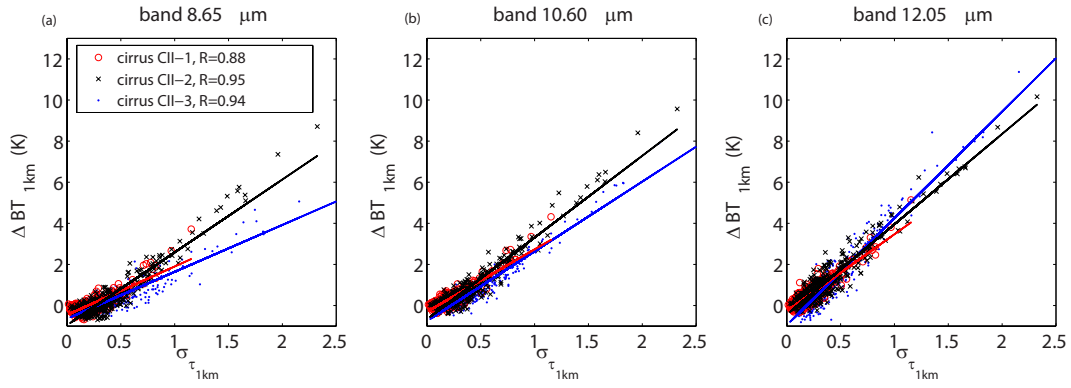

Figure 15. Brightness temperature differences, $\Delta BT_{1\,\mathrm{km}}$, viewed at the nadir as a function of the optical thickness standard deviation $\sigma_{\tau_{1\,\mathrm{km}}}$ for cirri CII-1, CII-2 and CII-3 and for the bands at 8.65 µm, 10.60 µm and 12.05 µm.

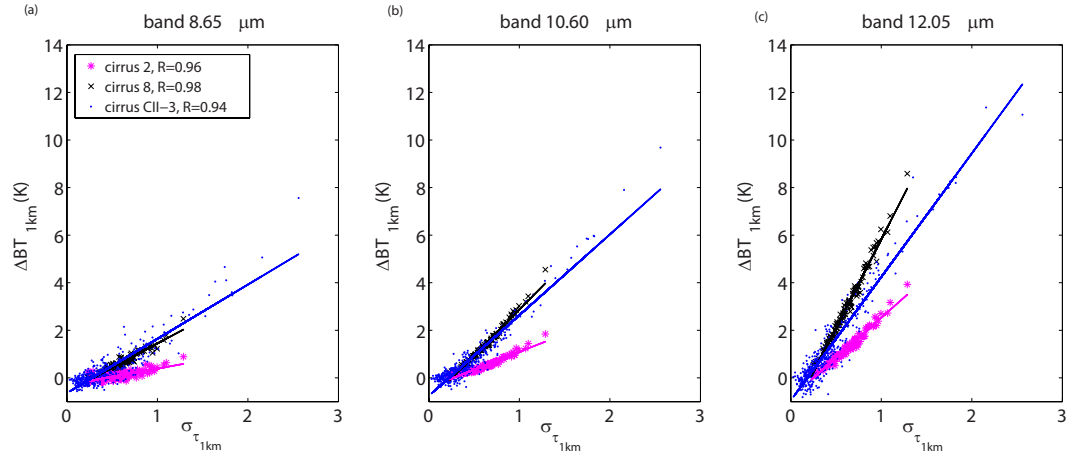

Figure 16. Brightness temperature differences, $\Delta BT_{1\,\mathrm{km}}$, viewed at the nadir as a function of the optical thickness standard deviation $\sigma_{\tau_{1\,\mathrm{km}}}$ for cirrus 2, cirrus 8 and CII-3 and for the bands at 8.65 µm, 10.60 µm and 12.05 µm. The cloud top of cirrus 2, cirrus 8 and cirrus CII-3 is 7.97 km, 11.06 km and 11.06 km, respectively, and the cloud base is at 7.60 km, 11.06 km and 9.06 km, respectively.

are highly absorbent in this band (Table 2). For the band at 8.65 µm, ϖ_0 is larger for small particles leading to more scattering which smoothes the radiative field heterogeneity. We can, thus, conclude that the optical property model has a weak influence on the heterogeneity effects on BT (in average inferior to 1 K) for IIR measurements. However, it could become significant for radiometers with a higher instrumental accuracy.

3.4 Influence of altitude and geometrical thickness of the cirrus cloud

In the troposphere, the temperature decreases with altitude. A cirrus with a high altitude emits, therefore, at a lower temperature than a cirrus with the same optical properties at a lower altitude. Figure 16 presents $\Delta BT_{1\,\mathrm{km}}$ as a function of $\sigma_{\tau_{1\,\mathrm{km}}}$ for cirrus 2 with the top altitude of 7.97 km and cirrus 8 and CII-3 with the top altitude of 11.06 km. We note that $\Delta BT_{1\,\mathrm{km}}$ is greater for the higher cirrus. Indeed, for a higher cloud, the BT contrast between the cloud top and the clear sky is larger leading to a stronger PPA bias.

To study the influence of the vertical extension, we then compare cirrus 8 and CII-3. They have the same optical characteristics, the same cloud top altitude but a different vertical extension involving a different cloud base at 9.06 km for cirrus CII-3 and at 10.60 km for cirrus 8. Note that the cirrus optical thickness distribution is also different but, as seen previously, it does not influence the $\Delta BT_{1\,\mathrm{km}}$ much. Figure 16 shows slight differences between the two clouds at 8.65 µm and at 10.60 µm but a greater difference at 12.65 µm. At this wavelength, the absorption is strong, leading to a large contrast between the cloud top and clear-sky brightness temperatures. However, the cloud base of cirrus CII-3 is at a lower altitude, meaning that the emission temperature is higher and, thus, closer to the surface temperature. The average temperature of cirrus CII-3 is, thus, forms less of a contrast with the surface temperature than cirrus 8 does, leading to a lower PPA bias. To conclude, for two identical cloud top altitudes,

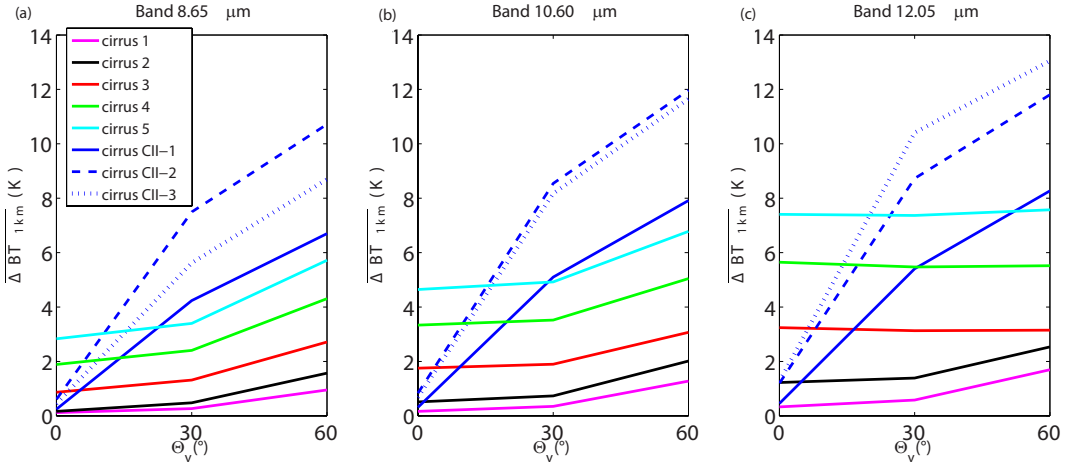

Figure 17. Mean difference $\overline{\Delta BT_{1\,\mathrm{km}}}$ as a function of the zenith view angle $\Theta_\mathrm{v}(°)$ for cirrus 1 to 5 and cirrus CII-1 & CII-2 for the bands at 8.65 µm, 10.60 µm and 12.05 µm.

if the band is strongly dominated by the absorption (as the band at 12.05 µm), the PPA bias decreases with the increase in the vertical extension, but this effect is, on average, on the order of tenths of a Kelvin.

3.5 Influence of the observation geometry on cloud heterogeneity effects

The previous results were presented for nadir view as measured by IIR/CALIPSO. In this section, heterogeneity effects for other view directions are investigated. In the framework of a 3-D radiative transfer for tilted geometry, photons cross different inhomogeneous columns (Tilted Independent Pixel Approximation (TIPA), Várnai and Davies, 1999) contrary to the 1-D framework which assumes infinite horizontal layers. Figure 17 shows the $\Delta BT_{1\,\mathrm{km}}$ averaged over all the pixels of the field ($\overline{\Delta BT_{1\,\mathrm{km}}}$) as a function of the zenith view angle Θ_v for cirrus 1 to 5 and for CII-1, CII-2 and CII-3 cirrus. For the band at 8.65 µm, the $\overline{\Delta BT_{1\,\mathrm{km}}}$ increases with Θ_v. For cirrus 1 to 5, $\overline{\Delta BT_{1\,\mathrm{km}}}$ is twice as large for $\Theta_\mathrm{v} = 60°$ than for $\Theta_\mathrm{v} = 0°$. For CII-1, CII-2 and CII-3 cirrus, the difference is approximately ten times as large because they present a greater 3-D variability of the extinction coefficient. In the band at 12.05 µm, we note for cirrus 3, cirrus 4 and cirrus 5 that the $\overline{\Delta BT_{1\,\mathrm{km}}}$ does not change as a function of Θ_v. This is due to a saturation effect. These three cirri have a large mean optical thickness ($\tau_\mathrm{c} = 1.8$), with optical thicknesses superior to 6 for some pixels. As we can see in Fig. 7, the PPA bias tends to zero for these pixels as the surface emission is not visible any more. We also note that, for $\Theta_\mathrm{v} \neq 0°$, $\overline{\Delta BT_{1\,\mathrm{km}}}$ is no longer correlated with $\sigma_{\tau_{1\,\mathrm{km}}}$, which is computed for integrated vertical cloud columns and, thus, does not represent the heterogeneity perceived from an oblique zenith view angle. Concerning view azimuth angle Φ_v, we see no real tendency, except for differences due to different crossed optical properties.

3.6 Influence of the observation scale on cloud heterogeneity effects

The previous results have been presented for the IIR spatial resolution of 1 km × 1 km. In this section, heterogeneity effects are presented for different spatial resolutions. Figure 18 shows the average brightness temperature difference $\overline{\Delta BT}$ as a function of the increase in the spatial resolution: 1 km, 2.5 km (only for cirrus 5 for time calculation reasons), 5 km, 10 km and 20 km (only for CII-1, CII-2 and CII-3 cirrus). For each spatial resolution, differences are computed between 3-D brightness temperatures, first calculated at 100 m and then averaged at the indicated spatial resolution, and brightness temperatures computed from the average of the optical properties at the scale of 1 km, 2.5 km, 5 km, 10 km or 20 km. The difference of brightness temperatures at each scale are then averaged over the whole cirrus to obtain $\overline{\Delta BT}$. We observe that the $\overline{\Delta BT}$ is maximal for cirrus 5, the most heterogeneous, with a value about 1.5 K at 12.05 µm. We also notice that, $\overline{\Delta BT}$ quickly increases between 1 km, 2.5 km and 5 km and reaches an asymptote after that. This increase is all the more important as the cirrus mean optical thickness and mean heterogeneity parameters are large.

4 Summary and conclusions

This paper presents results concerning the impact of cirrus cloud heterogeneities on top-of-atmosphere brightness temperatures ($\Delta BT_{1\,\mathrm{km}}$). Spatial radiometers such as IIR/CALIPSO and MODIS/AQUA measure top-of-atmosphere brightness temperatures at 1 km × 1 km and their operational algorithms use the IPA and the PPA to retrieve cirrus cloud properties. Different effects can result from this assumption. We have shown that the larger effect at the 1 km scale is the PPA. It depends on the absorption properties and

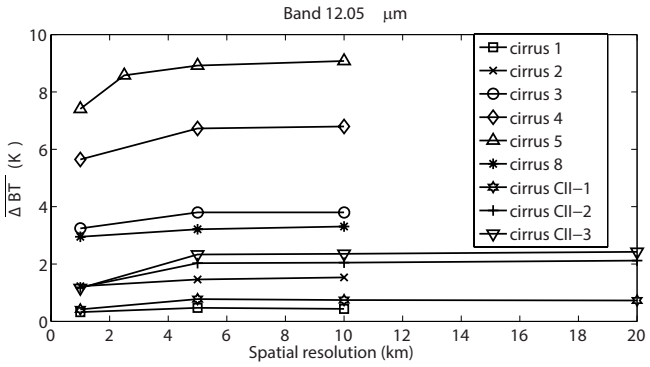

Figure 18. Brightness temperature differences $\overline{\Delta BT}$ at 12.05 µm as a function of the spatial resolution for different cirri.

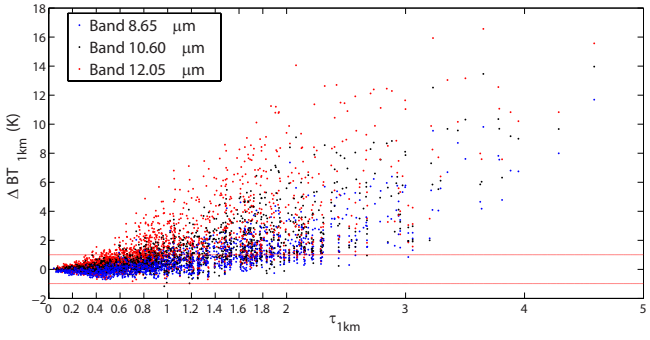

Figure 19. Brightness temperature differences, $\Delta BT_{1\,\mathrm{km}}$, viewed at the nadir between $BT3D_{1\,\mathrm{km}}$ and $BT1-D_{1\,\mathrm{km}}$ as a function of the optical thickness at 1 km ($\tau_{1\,\mathrm{km}}$) for the three channels of the IIR and for 2 000 pixels per band. The two red lines correspond to the instrumental accuracy of the IIR of about ±1 K.

therefore on the observation channel with larger effects for bands at 10.60 µm and 12.05 µm. We have also shown that $\Delta BT_{1\,\mathrm{km}}$'s depend mainly on the optical thickness standard deviation inside the observation pixel and on the brightness temperature contrast between the cloud top and the clear-sky atmosphere. Furthermore, the impact of heterogeneity effects increases strongly with the zenith view angle except for cirri with large mean optical thickness ($\tau_c = 1.8$), where a saturation effect is observed for the band at 12.05 µm due to the strong absorption.

To summarize the different results presented in this paper, Fig. 19 shows the brightness temperature differences, $\Delta BT_{1\,\mathrm{km}}$, simulated at the nadir as a function of the optical thickness at 1 km × 1 km ($\tau_{1\,\mathrm{km}}$). The two red lines correspond to the instrumental accuracy of IIR. The different cases of cirrus are superimposed to obtain 2 000 pixels with different optical thicknesses. For these cirri, the contrast between the cloud top and clear-sky brightness temperatures is between -46 K to -67 K and we observe that the heterogeneity effects start to be significant ($\Delta BT_{1\,\mathrm{km}}$ larger than the IIR instrumental accuracy of 1 K) around $\tau_{1\,\mathrm{km}} \sim 0.4$ at 12.05 µm. This is equivalent to $\tau_{1\,\mathrm{km}} \sim 0.3$ at 532 nm, corresponding to the limit of optically thick cirri defined by Sassen and Cho (1992). In terms of $\sigma_{\tau_{1\,\mathrm{km}}}$, heterogeneity effects are greater than 1 K for $\sigma_{\tau_{1\,\mathrm{km}}} \sim 1$.

We have also shown that heterogeneity effects increase strongly with the decrease of the spatial resolution until 10 km. Numerical weather prediction models assimilate cloudy radiances at 10 km resolution; it would be interesting to study the possibility of correcting the heterogeneity bias using, for example IIR, MODIS or Spinning Enhanced Visible and Infrared Imager (SEVIRI) information at 1 km.

The slight photon transport effect in the thermal infrared involves that heterogeneity effects are mainly due to the PPA bias. This bias should be easier to correct than 3-D effects as it could be estimated with subpixel heterogeneity or it could be decreased by reducing pixel size. However, photon transport effects increase when pixel size is reduced. For the IIR accuracy of 1 K, they become significant for spatial resolutions below 250 m. Assuming a 1 K radiometer accuracy, a spatial radiometer with a spatial resolution of 250 m × 250 m could retrieve cloud optical properties with weak PPA bias and weak 3-D effects.

In a future companion paper (Fauchez et al., 2014), we will focus on the estimation of the impact of cirrus heterogeneities on the cloud properties retrieved from IIR thermal infrared measurements with the 1-D approximation.

Acknowledgements. The authors acknowledge the Centre National de la Recherche Scientifique (CNRS), the Programme National de Télédétection Spatiale (PNTS) and the Direction Générale de l'Armement (DGA) for their financial support. We are also grateful for the use of resources provided by the European Grid Infrastructure. For more information, please refer to the EGI-InSPIRE paper (http://go.egi.eu/pdnon).

We thank Anthony Baran for the numerous fruitful discussions on the cirrus optical properties.

We also thank the two reviewers whose remarks greatly improved the quality of this article.

Edited by: B. Mayer

The publication of this article is financed by CNRS-INSU.

References

Baran, A. J.: From the single-scattering properties of ice crystals to climate prediction: A way forward, Atmos. Res., 112, 45–69, 2012.

Baran, A. J. and Labonnote, L.-C.: A self-consistent scattering model for cirrus. I: The solar region, Q. J. Roy. Meteor. Soc., 133, 1899–1912, 2007.

Baran, A. J., Connolly, P. J., and Lee, C.: Testing an ensemble model of cirrus ice crystals using midlatitude in situ estimates of ice water content, volume extinction coefficient and the total solar optical depth., J Quant. Spectrosc. Rad., 110, 1579–598, 2009.

Baran, A. J., Cotton, R., Furtado, K., Havemann, S., Labonnote, L.-C., Marenco, F., Smith, A., and Thelen, J.-C.: A self-consistent scattering model for cirrus. II: The high and low frequencies, Q. J. Roy. Meteor. Soc., 140, 1039–1057, doi:10.1002/qj.2193, 2014.

Baum, B., Yang, P., Heymsfield, A., Platnick, S., King, M., Hu, Y.-X., and Bedka, S.: Bulk scattering properties for the remote sensing of ice clouds. Part II. Narrowband models, J. Appl. Meteorol, 44, 1896–1911, 2005.

Baum, B., Yang, P., Heymsfield, A., Schmitt, C., Xie, Y., Bansemer, A., Hu, Y.-X., and Zhang, Z.: Improvements in shortwave bulk scattering and absorption models for the remote sensing of ice clouds, B. Am. Meteorol. Soc., 50, 1037–1056, 2011.

C. Labonnote, L., Brogniez, G., Doutriaux-Boucher, M., Buriez, J.-C., Gayet, J.-F., and Chepfer, H.: Modeling of light scattering in cirrus clouds with inhomogeneous hexagonal monocrystals. Comparison with in-situ and ADEOS-POLDER measurements, Geophys. Res. Lett., 27, 113–116, 2000.

Cahalan, R. F., Ridgway, W., Wiscombe, W. J., Bell, T. L., and Snider, J. B.: The Albedo of Fractal Stratocumulus Clouds, J. Atmos. Sci., 51, 2434–2455, 1994.

Carlin, B., Fu, Q., Lohmann, U., Mace, J., Sassen, K., and Comstock, J. M.: High cloud horizontal inhomogeneity and solar albedo bias, J. Climate, 15, 2321–2339, 2002.

Chen, Y. and Liou, K. N.: A Monte Carlo method for 3D thermal infrared radiative transfer, J Quant. Spectrosc. Rad., 101, 166–178, 2006.

Cooper, S. J., L'Ecuyer, T. S., Gabriel, P., Baran, A. J., and Stephens, G. L.: Performance assessment of a five-channel estimation-based ice cloud retrieval scheme for use over the global oceans, J. Geophys. Res. Atmos., 112, D04207, doi:10.1029/2006JD007122, 2007.

Cornet, C., Isaka, H., Guillemet, B., and Szczap, F.: Neural network retrieval of cloud parameters of inhomogeneous clouds from multispectral and multiscale radiance data: Feasibility study, J. Geophys. Res. Atmos., 109, D12203, doi:10.1029/2003JD004186, 2004.

Cornet, C., C-Labonnote, L., and Szczap, F.: Three-dimensional polarized Monte Carlo atmospheric radiative transfer model (3DMCPOL): 3D effects on polarized visible reflectances of a cirrus cloud, J. Quant. Spectrosc. Rad., 111, 174–186, doi:10.1016/j.jqsrt.2009.06.013, 2010.

Eguchi, N., Yokota, T., and Inoue, G.: Characteristics of cirrus clouds from ICESat/GLAS observations, Geophys. Res. Lett., 34, L09810, doi:10.1029/2007GL029529, 2007.

Emde, C., Buras, R., and Mayer, B.: ALIS: An efficient method to compute high spectral resolution polarized solar radiances using the Monte Carlo approach, J Quant. Spectrosc. Rad., 112, 1622–1631, 2011.

Evans, K. F.: The Spherical Harmonics Discrete Ordinate Method for Three-Dimensional Atmospheric Radiative Transfer., J. Atmos. Sci., 55, 429–446, 1998.

Fauchez, T., Dubuisson, P., Cornet, C., Szczap, F., Garnier, A., and J., P.: Impacts of clouds heterogeneities on the cirrus optical properties retrieved from spatial thermal infrared radiometry, Atmos. Meas. Tech. Discuss., in preparation, 2014.

Field, P. R., Hogan, R. J., Brown, P. R. A., Illingworth, A. J., Choularton, T. W., and Cotton, R. J.: Parametrization of ice-particle size distributions for mid-latitude stratiform cloud, Q. J. Roy. Meteor. Soc., 131, 1997–2017, 2005.

Field, P. R., Heymsfield, A., and Bansemer, A.: Snow size distribution parameterization for midlatitude and tropical ice clouds, J. Atmos. Sci., 64, 4346–4365, 2007.

Garnier, A., Pelon, J., Dubuisson, P., Faivre, M., Chomette, O., Pascal, N., and Kratz, D. P.: Retrieval of Cloud Properties Using CALIPSO Imaging Infrared Radiometer. Part I: Effective Emissivity and Optical Depth, J. Appl. Meteorol Clim., 51, 1407–1425, 2012.

Garnier, A., Pelon, J., Dubuisson, P., Yang, P., Faivre, M., Chomette, O., Pascal, N., Lucker, P., and Tim, M.: Retrieval of Cloud Properties Using CALIPSO Imaging Infrared Radiometer. Part II: effective diameter and ice water path, J. Appl. Meteorol Clim., 52, 2582–2599, 2013.

Hartmann, D. and Short, D.: On the use of earth radiation budget statistics for studies of clouds and climate, J. Atmos. Sci., 37, 1233–1250, 1980.

Henyey, L. G. and Greenstein, J. L.: Diffuse radiation in the galaxy, Ann. Astrophys., 3, 117–137, 1940.

Hogan, R. J. and Kew, S. F.: A 3D stochastic cloud model for investigating the radiative properties of inhomogeneous cirrus clouds, Q. J. Roy. Meteor. Soc., 131, 2585–2608, 2005.

Kratz, D. P.: The correlated k-distribution technique as applied to the AVHRR channels, J. Quant. Spectrosc. Rad., 53, 501–517, 1995.

Lacis, A. A. and Oinas, V.: A Description of the Correlated k Distribution Method for Modeling Nongray Gaseous Absorption, Thermal Emission, and Multiple Scattering in Vertically Inhomogeneous Atmospheres, J. Geophys. Res., 96, 9027–9063, 1991.

Lynch, D., Sassen, K., Starr, D., and Stephens, G.: Cirrus, Oxford University Press, USA, 1–25, 2002.

Magono, C.: Meteorological Classification of Natural Snow Crystals, Hokkaido University, 321–334, 1966.

Marshak, A. and Davis, A.: 3D radiative transfer in cloudy atmospheres, Physics of Earth and Space Environments Series, Springer-Verlag Berlin Heidelberg, 686 pp., 2005.

Mayer, B.: Radiative transfer in the cloudy atmosphere, Eur. Phys. J. Conf., 1, 75–99, 2009.

Mioche, G., Josset, D., Gaye, J., Pelon, J., Garnier, A., Minikin, A., and Schwarzenboeck, A.: Validation of the CALIPSO-CALIOP extinction coefficients from in situ observations in midlatitude cirrus clouds during the CIRCLE-2 experiment, J. Geophys. Res. Atmos., 115, 1–17, doi:10.1029/2009JD012376, 2010.

Ohring, G. and Clapp, P.: The Effect of Changes in Cloud Amount on the Net Radiation at the Top of the Atmosphere., J. Atmos. Sci., 37, 447–454, 1980.

Partain, P. T., Heidinger, A. K., and Stephens, G. L.: High spectral resolution atmospheric radiative transfer: Application of the equivalence theorem, J. Geophys. Res. Atmos., 105, 2163–2177, 2000.

Platnick, S., King, M. D., Ackerman, S. A., Menzel, W. P., Baum, B. A., Riedi, J. C., and Frey, R. A.: The MODIS cloud products: algorithms and examples from terra, IEEE Trans. Geosci. Remote Sens., 41, 459–473, 2003.

Sassen, K. and Cho, B. S.: Subvisual-Thin Cirrus Lidar Dataset for Satellite Verification and Climatological Research., J. Appl. Meteorol, 31, 1275–1285, 1992.

Sassen, K., Wang, Z., and D., L.: Global distribution of cirrus clouds from CloudSat/Cloud-Aerosol Lidar and Infrared Pathfinder Satellite Observations (CALIPSO) measurements, J. Geophys. Res. Atmos., 113, D00A12, doi:10.1029/2008JD009972, 2008.

Sourdeval, O., Brogniez, G., Pelon, J., C.-Labonnote, L., Dubuisson, P., Parol, F., Josset, D., Garnier, A., Faivre, M., and Minikin, A.: Validation of IIR/CALIPSO Level 1 Measurements by Comparison with Collocated Airborne Observations during CIRCLE-2 and Biscay '08 Campaigns, J. Atmos. Ocean. Technol., 29, 653–667, 2012.

Starr, D. and Cox, S.: Cirrus Clouds – Part II: Numerical Experiments on the Formation and Maintenance of Cirrus, J. Atmos. Sci., 42, 2682–2694, 1985.

Stephens, G. L.: Cloud Feedbacks in the Climate System: A Critical Review, J. Climate, 18, 237–273, 2005.

Stephens, G. L., Gabriel, P. M., and Tsay, S.-C.: Statistical radiative transport in one-dimensional media and its application to the terrestrial atmosphere, Transport Theor. Stat., 20, 139–175, 1991.

Szczap, F., Isaka, H., Saute, M., Guillemet, B., and Gour, Y.: Inhomogeneity effects of 1D and 2D bounded cascade model clouds on their effective radiative properties, Physics and Chemistry of the Earth, Hydrol. Ocean. Atmos., 25, 83–89, 2000.

Szczap, F., Gour, Y., Fauchez, T., Cornet, C., Faure, T., Joudan, O., and Dubuisson, P.: 3DCloud, a fast and flexible 3D cloud optical depth generator based on drastically simplified basic atmospheric equations and Fourier transform framework. Applications to stratocumulus, cumulus and cirrus cloud fields, Geosci. Model Dev. Discuss., in review, 2014.

Várnai, T. and Davies, R.: Effects of Cloud Heterogeneities on Shortwave Radiation: Comparison of Cloud-Top Variability and Internal Heterogeneity., J. Atmos. Sci., 56, 4206–4224, 1999.

Varnai, T. and Marshak, A.: Statistical analysis of the uncertainties in cloud optical depth retrievals caused by three-dimensional radiative effects, J. Atmos. Sci., 58, 1540–1548, 2001.

Wang, C., Yang, P., Baum, B., Platnick, S., Heidinger, A. K., Hu, Y., and Holz, R. E.: Retrieval of ice cloud optical thickness and effective size using a fast infrared radiative transfer model, J. Appl. Meteorol. Clim., 50, 2283–2297, 2011.

Winker, D. M., Vaughan, M. A., Omar, A., Hu, Y., Powell, K. A., Liu, Z., Hunt, W. H., and Young, S. A.: Overview of the CALIPSO Mission and CALIOP Data Processing Algorithms, J. Atmos. Ocean. Tech., 26, 2310, doi:10.1175/2009JTECHA1281.1, 2009.

Yang, P., Gao, B.-C., Baum, B. A., Hu, Y. X., Wiscombe, W. J., Tsay, S.-C., Winker, D. M., and Nasiri, S. L.: Radiative properties of cirrus clouds in the infrared (8-13 um) spectral region, J Quant. Spectrosc. Rad., 70, 473–504, 2001.

Yang, P., Wei, H., Huang, H.-L., Baum, B. A., Hu, Y. X., Kattawar, G. W., Mishchenko, M. I., and Fu, Q.: Scattering and absorption property database for nonspherical ice particles in the near- through far-infrared spectral region, Appl. Optics, 44, 5512–5523, 2005.